REPORT DOCUMENTATION PAGE

Form Approved
OMB No. 0704-0188

1. REPORT DATE *(DD-MM-YYYY)*	2. REPORT TYPE	3. DATES COVERED *(From - To)*
1/20/07	Final Technical Report	1/20/2003-6/30/2006

4. TITLE AND SUBTITLE
Microphysics of Air-Sea Exchanges

5a. CONTRACT NUMBER

5b. GRANT NUMBER
N00014-03-1-0384

5c. PROGRAM ELEMENT NUMBER

6. AUTHOR(S)
Brown, O. B.; Evans, R. H.; Donelan, M. A.; Minnett, P. J.; Ward, B.; McGillis, W. R.

5d. PROJECT NUMBER

5e. TASK NUMBER

5f. WORK UNIT NUMBER

7. PERFORMING ORGANIZATION NAME(S) AND ADDRESS(ES)
University of Miami
4600 Rickenbacker Causeway
Miami, FL 33149

Woods Hole Oceanographic Institution
Woods Hole, MA 02543, USA

8. PERFORMING ORGANIZATION REPORT NUMBER
667709 Final Report

9. SPONSORING/MONITORING AGENCY NAME(S) AND ADDRESS(ES)
Office of Naval Research
100 Alabama Street, SW
Suite 4R15
Atlanta, GA 30303

10. SPONSOR/MONITOR'S ACRONYM(S)
ONR

11. SPONSOR/MONITOR'S REPORT NUMBER(S)

12. DISTRIBUTION/AVAILABILITY STATEMENT
Approved for Public Release; distribution is unlimited

13. SUPPLEMENTARY NOTES

14. ABSTRACT
The objectives are to achieve a better understanding of the physics of the surface temperature structure and near-surface temperature gradients; specifically how they respond to different flux and wind regimes. An extensive set of measurements were taken in the Air-Sea Interaction Saltwater Tank (ASIST) at RSMAS under controlled conditions of wind speed and air-sea temperature difference to examine the behavior of the thermal skin layer. Air–water fluxes were controlled by changing the water temperature in the tank. Throughout the course of the experiment, air–water temperature differences were varied from ¬15 K to +15 K in increments of 5 K, and the wind speed was varied from 0 to 10 ms−1 in increments of 1 ms−1. Analysis has been undertaken in terms of the surface geometry, the subsurface temperature vertical microstructure, and the two-dimensional temperature variability at the water surface.

15. SUBJECT TERMS
Sea surface temperature, skin layer, air-sea fluxes, temperature microstructure, ASIST facility, flume experiments

16. SECURITY CLASSIFICATION OF:			17. LIMITATION OF ABSTRACT	18. NUMBER OF PAGES	19a. NAME OF RESPONSIBLE PERSON
a. REPORT	b. ABSTRACT	c. THIS PAGE			Peter Minnett
U	U	U		13	19b. TELEPHONE NUMBER *(Include area code)* (305)421-4104

Final report for ONR research grant

N00014-03-1-0384

Microphysics of Air-Sea Exchanges

O. B. Brown
Meteorology & Physical Oceanography
Rosenstiel School of Marine and Atmospheric Science
University of Miami
4600 Rickenbacker Causeway
Miami, FL 33149-1098
Phone: (305) 361-4000 Fax: (305) 361-4711
Email: obrown@rsmas.miami.edu

R. H. Evans
Meteorology & Physical Oceanography
Rosenstiel School of Marine and Atmospheric Science
University of Miami
4600 Rickenbacker Causeway
Miami, FL 33149-1098
Phone: (305) 361-4799 Fax: (305) 361-4622
Email: revans@rsmas.miami.edu

M. A. Donelan
Applied Marine Physics
Rosenstiel School of Marine and Atmospheric Science
University of Miami
4600 Rickenbacker Causeway
Miami, FL 33149-1098
Phone: (305) 361-4717 Fax: (305) 361-4701
Email: mdonelan@rsmas.miami.edu

P. J. Minnett
Meteorology & Physical Oceanography
Rosenstiel School of Marine and Atmospheric Science
University of Miami
4600 Rickenbacker Causeway
Miami, FL 33149-1098
Phone: (305) 361-4104 Fax: (305) 361-4622
Email: pminnett@rsmas.miami.edu

B. Ward
Applied Ocean Physics & Engineering,
Woods Hole Oceanographic Institution
Woods Hole, MA 02543, USA
Phone: (508) 289.3407 Fax: (508) 457-2194
Email: bward@whoi.edu

W. R. McGillis
Applied Ocean Physics & Engineering,
Woods Hole Oceanographic Institution
Woods Hole, MA 02543, USA
Phone: (508) 289-3325 Fax: (508) 457-2132
Email: wmcgillis@whoi.edu

Performance Period: January 20, 2003 – June 30, 2006

Total Funding: $333,397.82

LONG-TERM GOALS

The research efforts are targeted at improving our understanding of the microphysics of air-sea exchanges, especially the physics of the oceanic thermal skin and diurnally-influenced layers. This will lead to better assimilation of satellite-derived sea-surface temperature (SST) fields into meaningful climatologies and to more physically-based applications of satellite data to studies of air-sea interactions and to other naval applications. The constellation of satellites with infrared radiometers for SST measurements has a range of local over-pass times and, because of the diurnally forced fluctuation in SST and of the fluctuations of the skin effect in response to differing air-sea fluxes, this creates a problem in combining these fields into a reliable, consistent composite analysis. The results of this new research will improve the reliability of such composite analyses for naval applications.

OBJECTIVES

The objectives are to achieve a better understanding of the physics of the near-surface temperature gradients; specifically how they respond to different flux and wind regimes. This improved knowledge will be applied to providing a better, physically-based approach to time-compositing SST fields derived from infrared imaging radiometers on earth observation satellites.

APPROACH

An extensive set of measurements were taken in the Air-Sea Interaction Saltwater Tank (ASIST) at RSMAS under controlled conditions of wind speed and air-sea temperature difference to examine the behavior of the thermal skin layer. The measurements are comprehensive both in the extensive instrumentation brought to the experiments, and the wide range of imposed parameters.

During the ASIST Cool Skin Experiment, fresh water was used and the wind tunnel was in the open mode to allow steady state fluxes to be obtained. This pumped air at the ambient external temperature into the tank, which remained fairly constant for the two week experiment. Air–water fluxes were controlled by changing the water temperature. Throughout the course of the experiment, air–water temperature differences were varied from 15 K to +15 K in increments of 5 K, and the wind speed was varied from 0 to 10 ms^{-1} in increments of 1 ms^{-1}.

Table 1. A matrix of the experimental runs with wind speeds in the range of 0 to 10 ms^{-1} and air-water temperature differences of ±15K.

Wind	T_{air} - T_{water} (K)						
u (ms^{-1})	-15	-10	-5	0	5	10	15
0	x	x	x	x	x	x	x
1		x				x	
2	x	x	x	x	x	x	x
3	x	x	x		x	x	x
4	x	x	x	x	x	x	x
5	x		x		x	x	x
7	x	x	x	x	x	x	x
9	x					x	x
10	x	x	x	x	x	x	x

WORK COMPLETED

We are concerned with the mixing characteristics of the upper layer of the ocean and particularly with the very thin layer adjacent to the surface, in which rapid changes of temperature and dissolved contaminants distinguish it from the relatively well-mixed surface layers beneath. The wind acting on the surface provides the source of mechanical energy that mixes the upper layers, either through the breakdown of the shear layer generated by the tangential stress or through the direct injection of turbulence from the breaking of waves at and above the spectral peak of the wind-generated sea. The latter process has been shown to dominate once the wind speed exceeds the level of "incipient white-capping" or about 6 ms^{-1} at 10m height.

A set of ASIST experiments were done over a two week period in December 2001 (Table 1). All of the parameters that influence the thermal skin layer were measured directly in the ASIST with uncertainties <5%.

The skin temperature was measured using the Marine-Atmospheric Emitted Radiance Interferometer (M-AERI; Minnett *et al.*, 2001) looking down into flume, and two infrared imagers were mounted above the flume; one was operated by Dr G. Smith of NRL, as part of collaborative research, and the other was a new sensor at RSMAS, a FLIR Systems High Performance Thermal Imaging System SC 3000. This operates in the infrared spectral range of 8 to 9 μm and delivers imagery of the surface skin temperature with a relative accuracy of 0.02K.

The *in situ* gradients were measured by a new microthermometer (μT), an accurate thermistor (FP07) and a microconductivity (μC) sensor to determine the surface (Ward *et al.*, 2004). These were mounted on a vertical mast which was attached to a linear servo motor. Measurements were made from a depth of 13 cm to the surface at an ascent velocity of precisely 0.5 ms^{-1}, and at a repetition period of about 5 seconds. The sensors were mounted into J-shaped supports, shown in Figure 1. Profiling action was accomplished by mounting the sensors on the linear motor. Synchronization with other measurements was accomplished with a slow saw-tooth voltage, which was acquired on one of the A/D channels.

Infrared and visible video, laser systems and hot-film velocimetry were used to determine the flow fields below the interface.

Turbulent velocity fluctuations in the air were made with hot x-film anemometry and these were calibrated against pitot tubes over the full range of wind speeds used. Calibrations were done with the instruments *in situ* by ramping the fan speed up and down over 30 minutes. The momentum flux across the surface was estimated from direct eddy correlation measurements of these velocities recorded at 200 Hz. The hot films were kept in the turbulent boundary layer close to the surface and corrections for the stress gradient in the tank were made.

Temperature fluctuations were made with a fine ('cold') wire TSI constant current anemometer and these enabled direct eddy correlation measurements of the sensible heat flux. The humidity fluctuations were measured with a Li-Cor closed-path non-dispersive infra-red analyzer into which air was drawn at 12 liters/min through a 6mm diameter tube that sampled the air 5.3cm behind the x-films. The Li-Cor samples at 10Hz (5Hz Nyquist). The eddy correlation analysis of these data accounts for the time delay and dispersion in the sampling tube leading to the analyzer and also for the loss of flux carrying fluctuations between 5Hz and 100Hz. The latter is done by matching the measured latent heat fluxes in the measured range of 0-5Hz with universal curves (checked with the sensible heat flux

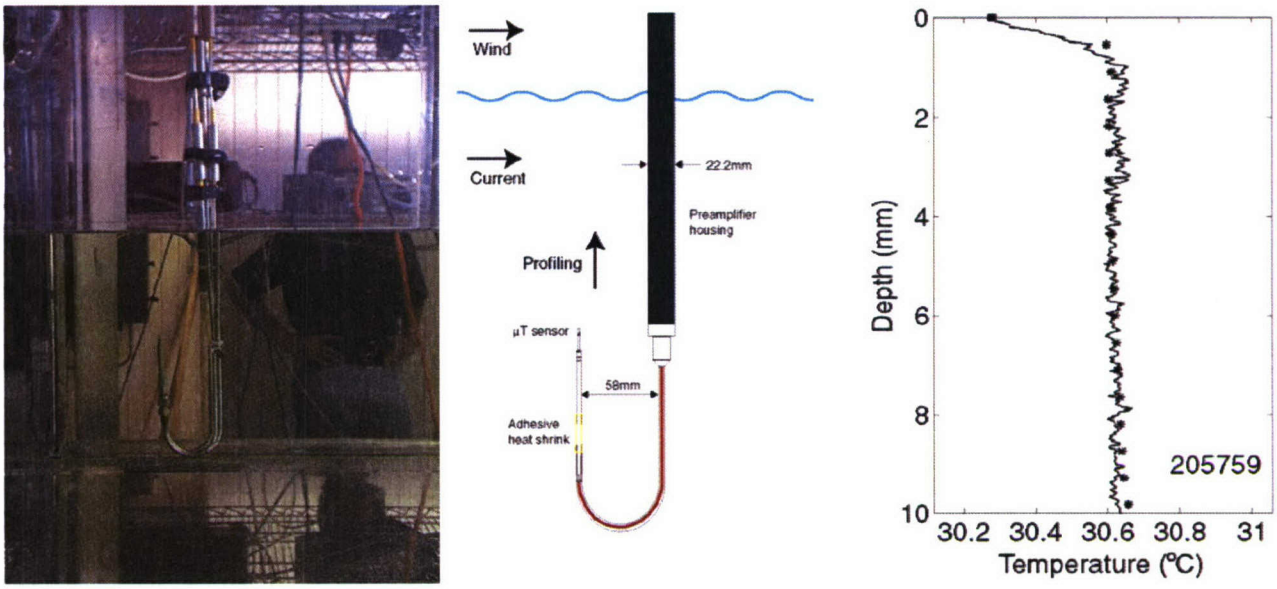

Figure 1. The thermometers used to profile the temperature in the ASIST. Left a photograph with the sensors at the deepest excursions; center is a schematic of the profiling rig; right is an example of the temperature profile measured by the microthemometer (solid), and a high-accuracy thermometer, at a lower vertical resolution (stars). The square symbol at zero depth represents the radiometric skin temperature measured by the M-AERI.

measurements) and adjusting the measured flux to account for the missing self-similar high frequency part. In this carefully controlled laboratory environment the fluxes of momentum, heat and moisture are expected to be accurate within 5%.

Wave heights, slopes and wavenumber (directional) spectra were determined using Laser Elevation Gauges (LEGs) and a 2-D Imaging Slope Gauge (ISG) so that wave propagation was not disturbed by intrusive measurement techniques. In the LEG system a line-scan CCD camera observes the vertical displacement of a laser generated bright spot on the water surface. This technique can resolve vertical displacements as small as 0.03 cm at up to a rate of 250 Hz. Three LEGs arranged in an equilateral triangle of side 1 cm were used to determine elevations, slopes and wavenumber spectra in the manner devised by Donelan *et al.*, (1996). Spectra having wavelengths as small as 2 cm are resolved.

The principal tool for observing the subsurface turbulence structure was Digital Particle Image Velocimetry (DPIV). The measurements were made with a DPIV system manufactured by Dantec. In this Lagrangian flow measurement technique the flow is "seeded" with 10 micron neutrally buoyant spheres and a double flash laser system illuminates the flow at 15 Hz with about 1 ms between the members of the pairs of flashes. These image pairs are captured on a CCD camera and cross-correlated in sub-areas of the 10^6 pixel matrix yielding a "map" of velocity vectors in a 62 x 62 matrix at 15 Hz. In this 2-D system only the projections of the vectors in a vertical plane parallel to the tank's long axis are obtained, although other choices are possible. The area selected was 75.5 mm x 75.5 mm and so the vectors were obtained at a spacing of 1.22 mm. This is an order of magnitude larger than the expected Kolmogorov microscale, but two orders of magnitude smaller than the breaking waves,

which are believed to be the principal source of turbulent energy in the "wave zone". This wide range between assumed input scales and those responsible for dissipation to heat augurs well for a defined inertial sub range (ISR), in which the structure function increases as the 2/3 power of the separation distance between velocity pairs according to the Kolmogorov similarity law (see, for example, Dickey and Mellor., 1979).

RESULTS

Surface geometry

Several field experiments have shown a sudden increase in the mass transfer velocity of slightly soluble contaminants when the wind exceeds the level of "incipient white-capping" or about 6 ms^{-1} at 10m height, and laboratory experiments have linked mass transfer velocity and mean square slope (*mss*) of the waves. Of course, the *mss* does not directly mix the surface fluid but it may be an effective indicator of the rate of wave breaking and therefore the kinetic energy dissipation rate induced by wave breaking.

Our measurements permit us to examine the connection between *mss* and turbulent kinetic energy dissipation, ε. The *mss* was estimated from surface elevation measurements at three points obtained using a laser elevation gauge (LEG). The LEG measures the surface elevation at a point by tracking the intersection of a laser beam with the surface using a line scan digital camera. A small quantity of fluorescein in the water causes laser-induced fluorescence and a distinct change in the scattered light above and below the surface.

The measurements of ε were obtained with hot-film anemometry at a depth of 6cm. A miniature wedge probe was overheated by about 10 K and recorded at 200 Hz. The level of the spectrum of the downstream component of velocity in its inertial sub-range just below the wave peak was used to estimate ε. Figure 2 compares the *mss* with ε [m^2s^{-3}]. The solid line represents $\varepsilon = 0.0545\ mss^2$and is almost indistinguishable from the (dashed) linear regression line in logarithmic coordinates.

To make a physically meaningful connection between *mss* and ε we note that the latter reflects the loss of energy from the wave field through breaking, whereas *mss* may be a good statistical measure of the incidence of breaking (steep waves) per unit area. The energy lost in each breaking event is therefore related to the loss of potential energy from the crest of the breaker or *gh*, where *h* is the crest height. Since wave breaking occurs in a very narrow range of slopes, the energy loss per breaker may be expressed in terms of the wavelength (λ) of the breaking wave: $g\lambda$. The rate of breaking for a given *mss* will depend on the frequency of the breaking wave, ω as was shown by Donelan *et al.*, 1972. Consequently the rate of energy loss from breaking, É, may be expressed in terms of these variables:

$$\acute{E} \sim mss\ g\ \lambda\ \omega$$

Figure 3 shows the correlation between É and the measured ε at 6cm depth:

$$\varepsilon = 9.3 \times 10^{-5}\ (mss\ g\ \lambda\ \omega)^{1.75}$$

The Imaging Slope Gauge (ISG) used a uniform light source underneath the test section shone through a mask with known gradients in red, green and blue intensities. The light then passed through a Fresnel lens that focused all light that has the same slope on the same point of the mask. This then allowed an RGB camera to directly observe the water surface slope through the relative intensities of the three color components at each point of the image. The ISG imaged an area of the water surface of up to 45

cm (downwind) x 30 cm (crosswind) at a resolution of 640 x 240. These images are sampled at a rate of 120 Hz using two interleaved RBG cameras. Collection of images was triggered by the M-AERI acquisition cycle and continued for a period of 4 seconds for each run. The total mean square slope of all images at all pixels for each run was compared with the wind speed (Figure 3). Although there was considerable scatter the general trend was a linear increase with wind speed above 2 ms^{-1} as expected. The spatial distribution of the slopes was typically randomly distributed about the mean value. However, for several of the runs there were spatially inhomogeneous mean square slopes (Figure 4). Bands of alternating high and low mean square slopes were observed aligned with the wind direction (Figure 5).

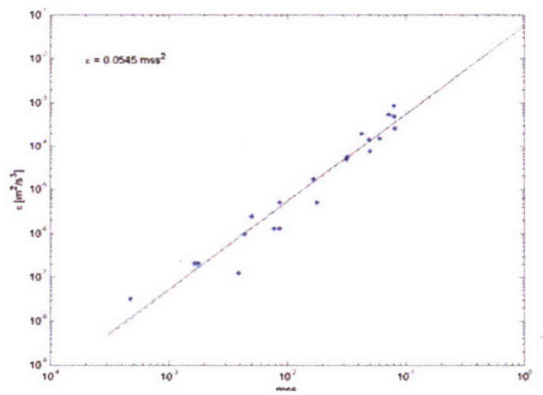

Figure 2. Measured turbulent kinetic energy dissipation, ε vs mean square slope of the waves, mss.

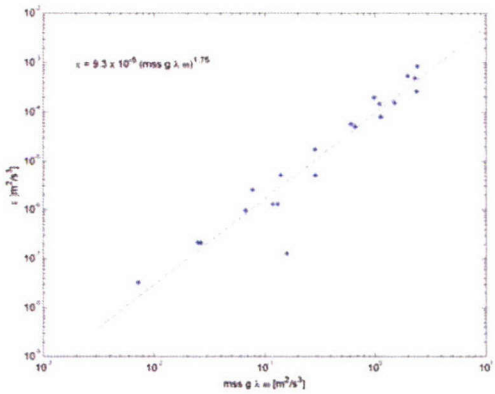

Figure 3. ε vs mss with dimensional consistency provided by the gravitational acceleration and the relevant wave properties: wavelength, λ and radian frequency, ω.

Vertical temperature structure

High-resolution thermometric measurements were conducted with the microthermometer, capable of resolving the viscous boundary layer. Figure 6 shows three consecutive runs taken under similar heat flux conditions, with the heat flux into the water. In Figure 6a the wind speed was 1 ms^{-1} and the thermometric measurements show a ΔT of 0.3 K. The conditions reflect a nighttime situation, with the absence of any stratification in the water column. In Figure 6b the wind speed is at 3 ms^{-1}, and the thermometric ΔT is reduced to about 0.15 K. The wind speed is increased to 5 ms^{-1} (Figure 6c), and the average water temperature has decreased by 0.8 K i.e. from about 14.3 to about 13.5 °C. The microthermometer ΔT is about 0.08 K.

The temperature drop across the molecular boundary layer is linear with depth, and a straight line through the temperature drop shows a boundary layer thickness of about 2 mm for the lowest wind speed. For the two higher wind speeds, the thickness of the sub-layer is approximately 1 mm. The fact that the thickness does not scale with wind speed may be due to the small heat flux increase in run 12 with the decrease in water temperature.

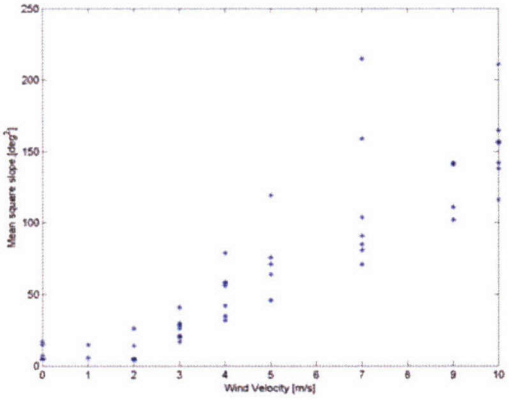

Figure 4. Mean Square along-tank slope as observed by the Imaging Slope Gauge. MSS given in units of deg^2. The air-sea temperature difference varies from -15 to +15 K for these runs.

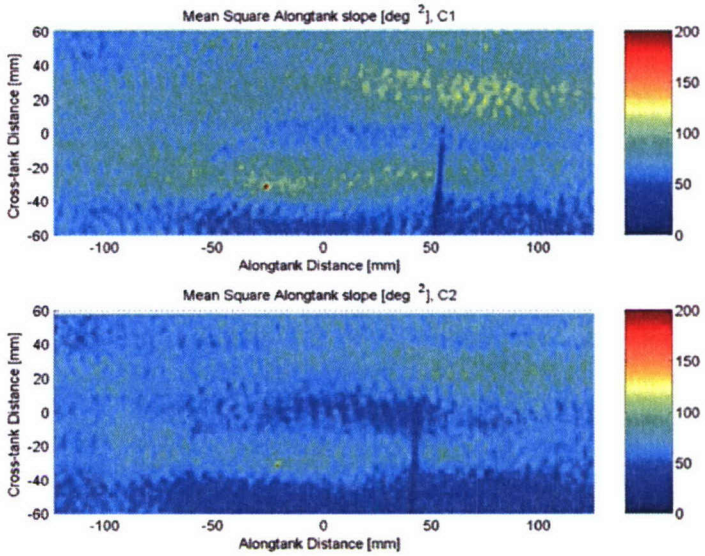

Figure 5 Mean square along-tank slope at each pixel as observed by the ISG. Wind speed was 4 ms^{-1} from right to left in these images. $T_{air} - T_{sea}$ was -10 K. The line in the image is due to either a scratch or a wrinkle in the film covering the opening.

Figure 7 shows a different situation, where the direction of the heat flux is out of the water providing a cooler skin than the bulk. However, the absolute value of the air-water temperature difference is smaller than the situation presented in figure 5, and the wind speeds are higher. The microthermometer ΔTs are 0.2 K, 0.17 K, 0.05 K, and 0.05 K, respectively. During these four runs, the M-AERI skin temperature remains invariant at 30.2 °C, whereas the average bulk temperature varies by a few tenths of a degree.

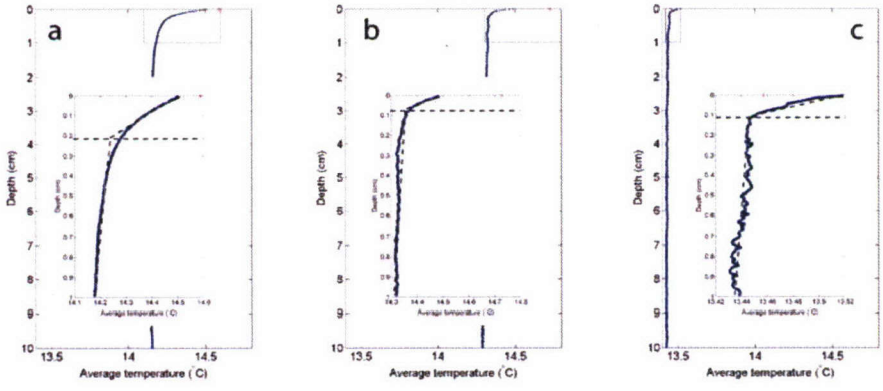

Figure 6. Averaged temperature profiles taken with air-water temperature difference of +10 K. The wind speeds were 1, 3, and 5 ms^{-1}, respectively. The overlaid plot in each subplot is that of the upper 10mm denoted by the box. The asterisk in each subplot represents the M-AERI skin temperature.

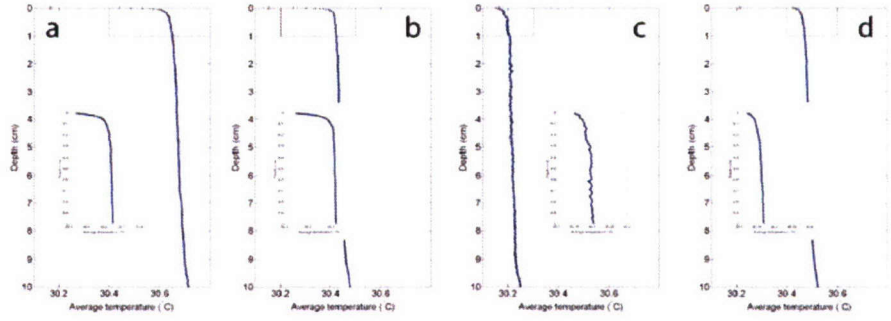

Figure 7. Averaged temperature profiles taken with air-water temperature difference of -5 K. The wind speeds were 4, 5, 7, and 10 ms^{-1}, respectively.

Figure 8 shows an average of all the profiles acquired during run10. This shows the skin layer thickness, δ, and the skin layer temperature difference, ΔT, derived from the data. Also shown is the skin temperature measurement from the M–AERI. From this, the air–water heat flux Qn can be estimated according to the Fourier Law of heat conduction:

$$Q_n = \Delta T k / \delta \qquad (1)$$

where k is the thermal conductivity of water 0.58 $Wm^{-1}K^{-1}$.

Figure 9 shows average profiles from two runs (see also Table 2). For the stable heat flux conditions of run 11, the net heat flux according to (1) was calculated to be 110.5 Wm^{-2}, compared to the bulk formulae value of 184.4 Wm^{-2}, using Stanton and Dalton numbers after Ocampo-Torres and Donelan (1994). There was an unstable heat flux for run 27, and the corresponding values for the profiler and bulk algorithm were 205.4 Wm^{-2} and 539 Wm^{-2}, respectively.

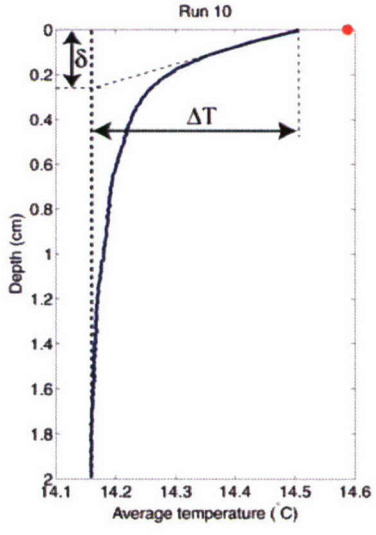

Figure 8. Average of profiles taken during run 10. The thickness of the molecular boundary layer is δ, and ΔT the temperature drop across it. The red data point is the skin temperature measured by M–AERI.

Table 2: Conditions during the runs and calculated profile parameters.

Run	u (ms^{-1})	Ta − Tw (K)	δc (mm)	ΔT (K)
11	3	10	0.7	0.16
27	5	- 5	0.35	0.17

Horizontal temperature structure

A FLIR Systems High Performance Thermal Imaging System SC 3000 was used in the experiment to take infrared images of the water surface in the ASIST tank. The SC 3000 measures in spectral range of 8 to 9 μm and delivers thermal imagery with a relative accuracy of 0.02K. The infrared imagery of the water surface was used to study the spatial variability of surface skin temperature on scales from

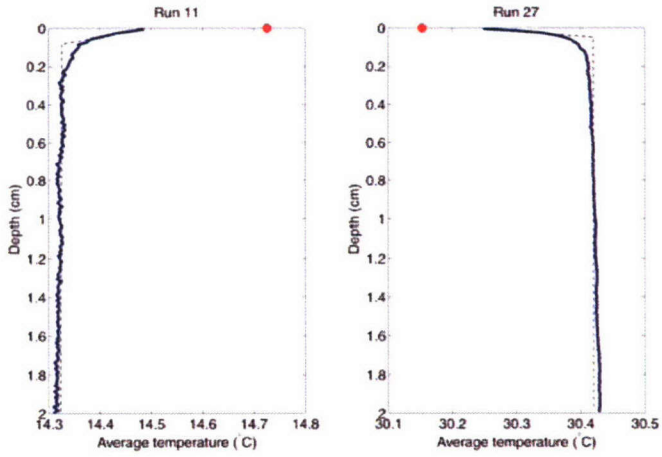

Figure 9. Average profiles for runs 11 and 27.

0.1 to 30 cm for a range of wind speeds and air-sea temperature differences (ΔT_{as}) that simulated different heat flux regiments.

The horizontal variability of skin temperature fluctuations is strongly related to the sign of the air-sea temperature difference which also determines the direction of sensible heat flux (in or out of the water) and is a controlling factor in determining the stability of the atmospheric boundary layer. This suggests that different mechanisms are involved in formation and maintenance of the skin layer depending on the sign of ΔT_{as}.

The infrared images of the water surface were analyzed to determine the spatial variability of the surface skin temperature on scales from 0.1 to 30 cm for a range of wind speeds and air-sea temperature differences. In particular, we a) examined the shape of the SST probability distribution function and its dependence on the air-sea temperature difference and the wind speed and b) used the infrared imagery to identify and study the skin layer temperature difference (skin SST – bulk SST) and wind speed dependence of the size of coherent structures in the temperature of the water surface.

Figure 10 shows examples of the skin SST images obtained for both negative and positive air-water temperature difference at zero wind speed. The size of each image is approximately 30x20 cm. The corresponding histograms of the SST in the scenes are also shown. The corresponding information for wind speeds of 4 ms^{-1} is shown in Figure 11. Our study showed that the shape of the SST probability distribution function depends strongly on the sign of the air-sea temperature difference and the wind speed. Figure 12 shows the scatter plots of the skewness of the skin SST probability density function versus the total heat flux $Q_H + Q_L$, where Q_H is the sensible and Q_L is the latent heat flux. There is a clear dependence between the heat fluxes and the skewness of the SST distribution. Large positive fluxes of either sensible or latent heat are accompanied by large negative skewness of the PDF and large negative fluxes by large positive skewness (Figure 12).

We investigated how the spatial variability of the SST in infrared imagery varies with the air-sea temperature difference and the wind speed. In particular, we examined the shape of the SST probability distribution function and its dependence on the ΔT_{as} and the wind speed (Figure 13).

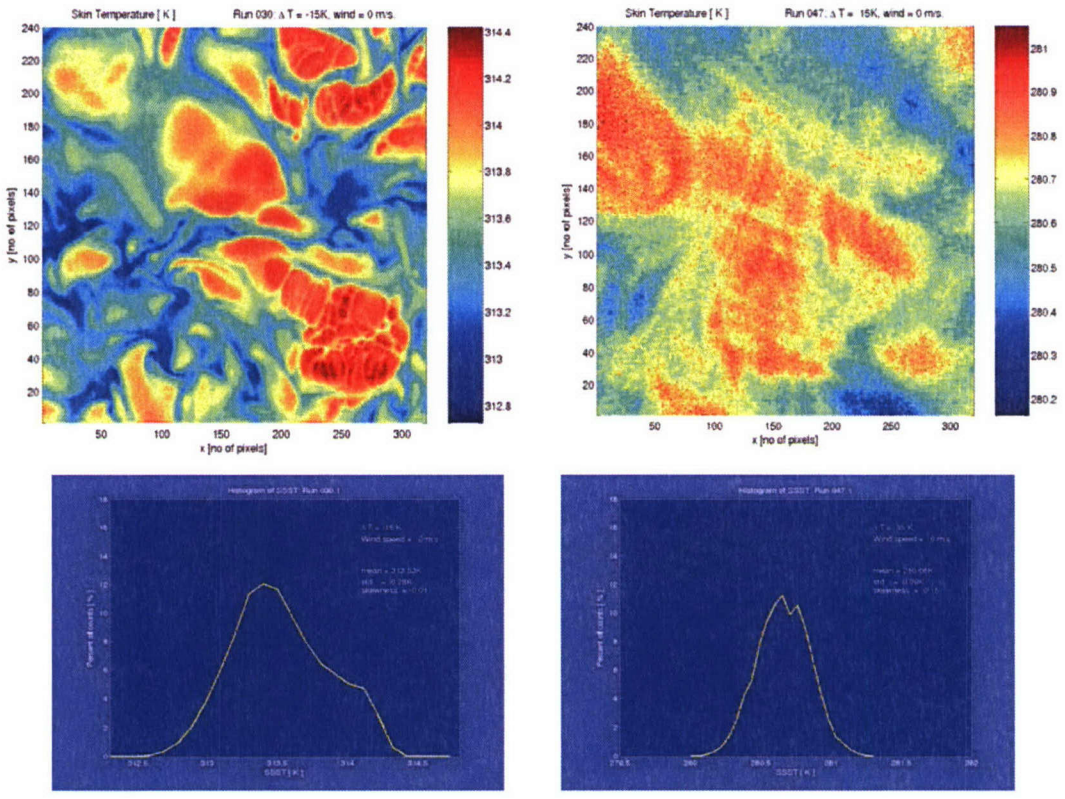

Figure 10 Images of the skin temperature for zero wind speed and air-water temperature differences of 15K: air cooler than water (top left) and air warmer than water (top right). Histograms of the skin temperature are shown below.

Images shown in Figures 10 and 11 also indicate the existence of coherent structures in the field of SST. Second order structure function (SF) analysis was employed to investigate spatial correlations in the images of SST. Figure 14 shows SFs obtained for SST fluctuations at ΔT= -10K and 10K. There is a striking difference in the behavior of the SST fluctuations at small scales between cases with positive and negative ΔT. For $\Delta T<0$ the slope of the SF at small scales is in most cases > 1 indicating persistent correlation. In turn, cases with $\Delta T>0$ show SFs with slopes < 1 implying antipersistent fluctuations. A systematic behavior of the SF with wind speed at small scales is also observed.

SUMMARY

Using unique resources and instrumentation, and novel analysis techniques we have undertaken a systematic investigation of the physics of the air-sea interface. This revealed some interesting and potentially important relationships. The Planning Letter to continue the analysis and to extend the experiment to measurements over the open ocean resulted in a recommendation not to submit a proposal. As a result the analysis of the data in hand has been curtailed through lack of funding.

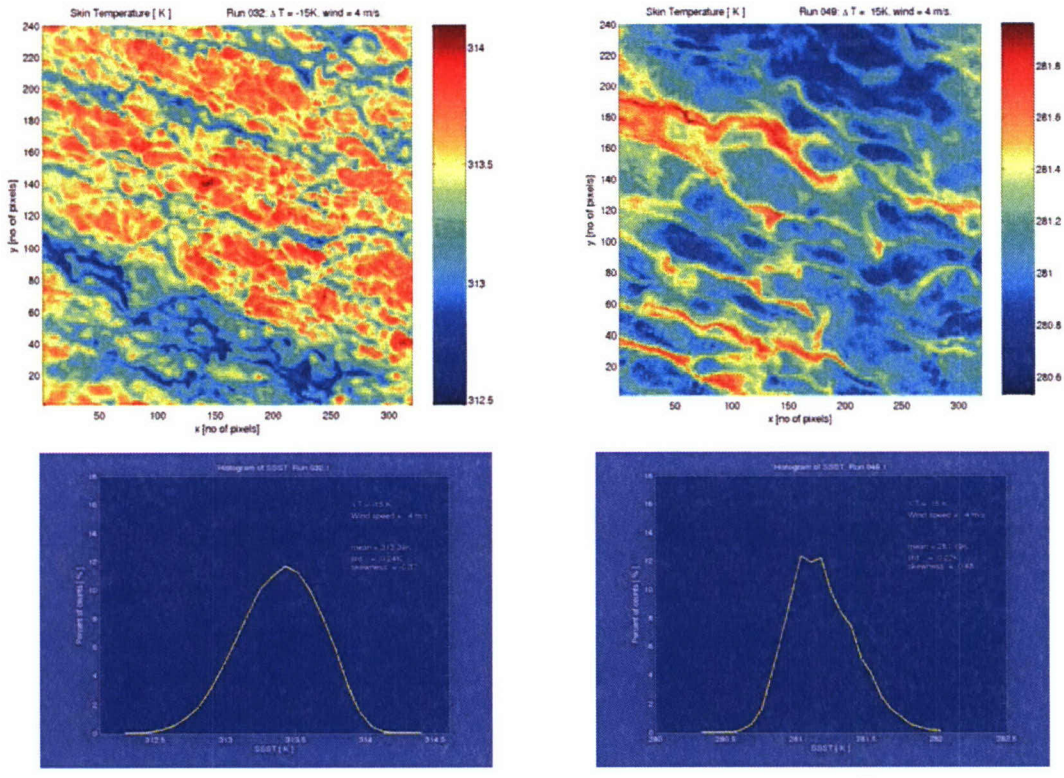

Figure 11. As figure 10, but for a wind speed of 4 ms^{-1}.

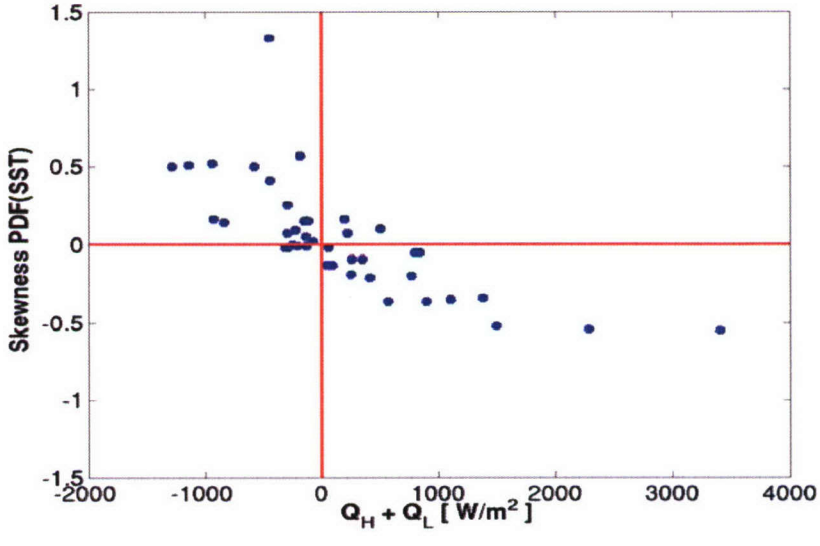

Figure 12. Skewness of the PDF of SST as a function of total heat flux ($Q_H + Q_L$).

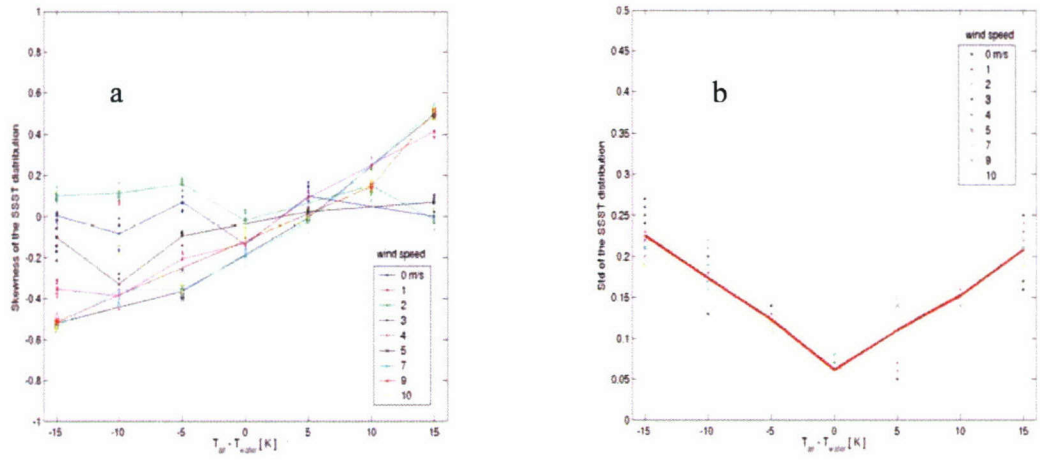

Figure 13. The skewness a) and standard deviation b) of SST distribution plotted against the air-sea temperature difference. Different values of wind speed are indicated by color symbols. The red line in b) represents average values for each ΔT_{as}.

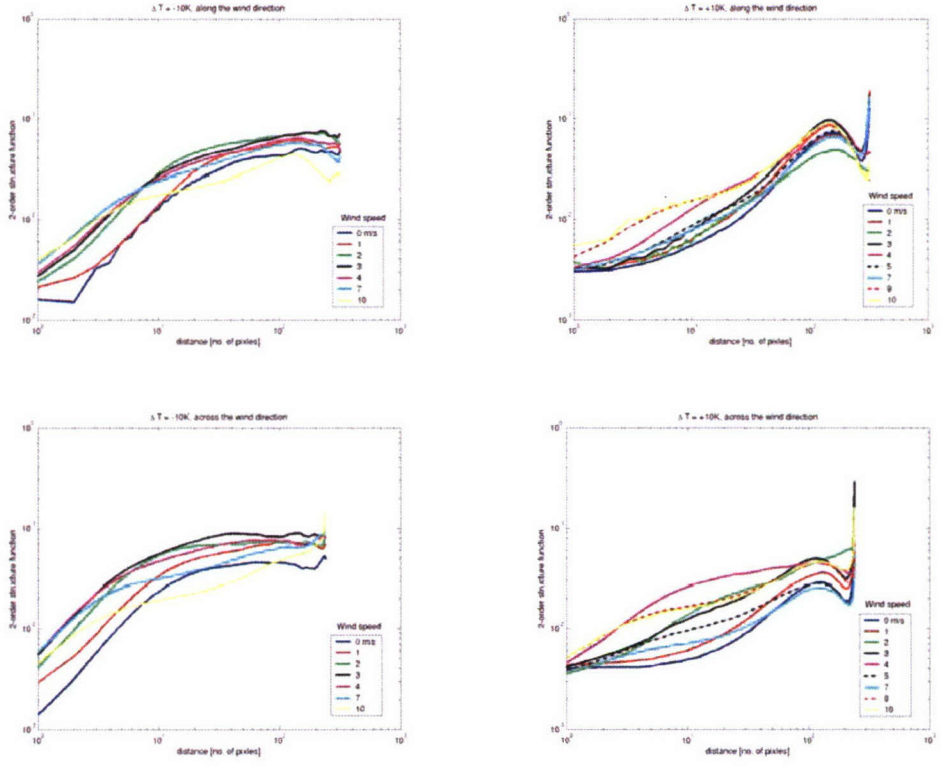

Figure 14. Second order structure functions of SST fluctuations along and across the wind direction in scenes with ΔT_{as} <0 (a and b) and ΔT_{as} >0 (c and d) at a range of wind speeds. (1 pixel ~ 1mm).

RELATED PROJECTS

This project has benefited from related research being done in the Remote Sensing Group at RSMAS with funding from other federal agencies, specifically instrument development through contracts and grants from NASA and NOAA. The ASIST facility was developed with funding from ONR, DURIP.

PUBLICATIONS

Ward, B. and M. A. Donelan, 2006: Thermometric measurements of the molecular sublayer at the air-water interface. *Geophysical Research Letters*, **33,** L07605. doi:10.1029/2005GL024769

PRESENTATIONS

Szczodrak, M., P.J. Minnett and M.A. Donelan. Centimeter Scale Variability of Water Surface Skin Temperature: Results from a Wave Tank Experiment, European Geophysical Union Meeting, Nice, France, 2004.

Szczodrak M., P.J. Minnett, M.A. Donelan, B.Haus, and B. Ward. Heat fluxes across the water surface and the variability of the surface skin temperature: results from a wave tank experiment. 37th International Liège Colloquium on Ocean Dynamics Gas Transfer at Water Surfaces, May, 2005.

Ward, B., P. J. Minnett, and M. A. Donelan. Skinlayer profiles in a wind–wave tank under various heat flux regimes, in EOS Trans. AGU 84(52), Ocean Sciences Meet. Suppl., Portland, USA, 2004. Abstract OS 41I06.

REFERENCES

Dickey, T. D. and G. L. Mellor., 1979: The Kolmogoroff r $^{2/3}$ Law. *Phys. Fluids.*, **22,** 1029-1032.

Donelan, M. A., M. S. Longuet-Higgins, and J. S. Turner, 1972: Whitecaps. *Nature*, **239,** 449-451.

Donelan, M. A., W. M. Drennan, and A. K. Magnusson, 1996: Nonstationary Analysis of the Directional Properties of Propagating Waves. *J. Phys. Oceanography*, **26,** 1901-1914.

Minnett, P. J., R. O. Knuteson, F. A. Best, B. J. Osborne, J. A. Hanafin, and O. B. Brown, 2001: The Marine-Atmospheric Emitted Radiance Interferometer (M-AERI), a high-accuracy, sea-going infrared spectroradiometer. *Journal of Atmospheric and Oceanic Technology*, **18,** 994-1013.

Ocampo-Torres, F. J. and M. A. Donelan, 1994: Laboratory measurements of mass transfer of carbon dioxide and water vapour for smooth and rough flow conditions. *Tellus*, **46B,** 16-32.

Ward, B., R. Wanninkhof, P. J. Minnett, and M. J. Head, 2004: SkinDeEP: A Profiling Instrument for Upper Decameter Sea Surface Measurements. *Journal of Atmospheric and Oceanic Technology*, **21,** 207-222.